Formaldehyde evolution in U.S. wildfire plumes during FIREX-AQ

Jin Liao[1,2], Glenn M. Wolfe[1], Reem A. Hannun[1,3], Jason M. St. Clair[1,3], Thomas F. Hanisco[1], Jessica B. Gilman[4], Aaron Lamplugh[4,5], Vanessa Selimovic[6], Glenn S. Diskin[7], John B. Nowak[7], Hannah S. Halliday[8], Joshua P. DiGangi[7], Samuel R. Hall[9], Kirk Ullmann[9], Christopher D. Holmes[10], Charles H. Fite[10], Anxhelo Agastra[10], Thomas B. Ryerson[4,*], Jeff Peischl[4,5], Ilann Bourgeois[4,5], Carsten Warneke[4], Matthew M. Coggon[4,5], Georgios I. Gkatzelis[4,5,**], Kanako Sekimoto[11], Alan Fried[12], Dirk Richter[12], Petter Weibring[12], Eric C. Apel[9], Rebecca S. Hornbrook[9], Steven S. Brown[4], Caroline C. Womack[4,5], Michael A. Robinson[4,5], Rebecca A. Washenfelder[4], Patrick R. Veres[4], J. Andrew Neuman[4,5]

[1]Atmospheric Chemistry and Dynamics Laboratory, NASA Goddard Space Flight Center, Greenbelt, MD, USA
[2]Universities Space Research Association, Columbia, MD, USA
[3]Joint Center for Earth Systems Technology, University of Maryland Baltimore County, Baltimore, MD, USA
[4]NOAA Chemical Science Laboratory (CSL), Boulder, CO, USA
[5]Cooperative Institute for Research in Environmental Science (CIRES), University of Colorado, Boulder, CO, USA
[6]Department of Chemistry, University of Montana, Missoula, MT, USA
[7]NASA Langley Research Center, Hampton, VA, USA
[8]Environmental Protection Agency, Durham, NC, USA
[9]Atmospheric Chemistry Observations & Modeling Laboratory, National Center for Atmospheric Research, Boulder, CO, USA
[10]Earth, Ocean and Atmospheric Science, Florida State University, FL, USA
[11]Yokohama City University, Japan
[12]Institute of Arctic and Alpine Research (INSTAAR), University of Colorado, Colorado, USA.
*now at Scientific Aviation, Boulder, Colorado, USA.
**now at Forschungszentrum Jülich GmbH, Julich, Nordrhein-Westfalen, DE, Germany.

Correspondence to: Jin Liao (jin.liao@nasa.gov)

Abstract. Formaldehyde (HCHO) is one of the most abundant non-methane volatile organic compounds (VOCs) emitted by fires. HCHO also undergoes chemical production and loss as a fire plume ages, and it can be an important oxidant precursor. In this study, we disentangle the processes controlling HCHO by examining its evolution in wildfire plumes sampled by the NASA DC-8 during the FIREX-AQ field campaign. In nine of the twelve analyzed plumes, dilution-normalized HCHO increases with physical age (range $1 - 6$ h). The balance of HCHO loss (mainly via photolysis) and production (via OH-initiated VOC oxidation) seems to control the sign and magnitude of this trend. Plume-average OH concentrations, calculated from VOC decays, range from -0.5 ($\pm$ 0.5) $\times$ 10^6 to 5.3 (±0.7) $\times$ 10^6 cm^{-3}. The production and loss rates of dilution-normalized HCHO seem to decrease with plume age. Plume-to-plume variability in dilution-normalized secondary HCHO production correlates with OH abundance rather than normalized OH reactivity, suggesting that OH is the main driver of fire-to-fire variability in HCHO secondary production. Analysis suggests an effective HCHO yield of 0.33 ($\pm$ 0.05) per VOC molecule oxidized for the 12 wildfire plumes. This finding can help connect space-based HCHO observations to the oxidizing capacity of the atmosphere and to VOC emissions.

1. Introduction

Wildfire biomass burning is a large source of trace gases and aerosols that affect regional atmospheric chemistry, human health, air quality, radiative balance and climate. Wildfire frequency and intensity are expected to increase with global warming under higher temperatures and drier conditions in the future (Westerling et al., 2006). Wildfire emissions of volatile organic compounds (VOCs) are a complex mixture spanning orders of magnitude in concentration, reactivity, and volatility (Gilman et al., 2015; Koss et al., 2018). These VOCs contribute to increased regional tropospheric ozone (Alvarado et al., 2010; Jaffe and Wigder, 2012; Mauzerall et al., 1998; Wotawa and Trainer, 2000) and can deposit onto or evaporate from organic aerosols in biomass burning air masses (Garofalo et al., 2019; Majdi et al., 2019; Palm et al., 2020).

Formaldehyde (HCHO) is one of the most abundant non-methane VOCs emitted by wildfires (Akagi et al., 2011; Gilman et al., 2015; Simpson et al., 2011). HCHO emissions vary with total carbon emissions, modified combustion efficiency (MCE) and fuel type. Emission factors of HCHO decrease as MCE increases (e.g., Liu et al., 2017; Yokelson et al., 1999), indicating that more HCHO is produced from smoldering fires than from flaming fires. HCHO emissions can vary by more than a factor of 2 among tropical forest, savanna, boreal forest and temperate forest biomes (Akagi et al., 2011). In addition to direct emissions, HCHO is formed in fire plumes via VOC oxidation. Alvarado et al. (2020) used TROPOMI data to show that HCHO enhancements in wildfire plumes persist for days downwind. HCHO also serves as an important source of peroxy radicals (HO_2), thereby influencing the formation of ozone and other secondary pollutants (Yokelson et al., 1999).

Few studies have investigated the photochemical evolution of HCHO in biomass burning plumes, and these studies have reported both net HCHO production and loss. Mauzerall et al. (1998) reported average HCHO enhancement ($\Delta HCHO/\Delta CO$) of 9.5 ppt/ppb for fresh plumes (less than 0.5 day), 1.8 ppt/ppb for recent plumes (less than 1 day), 2.3 ppt/ppb for aged plumes (< 5 days old), and 0.9 ppt/ppb for old plumes (>5 days old). Trentmann et al. (2005) observed a potential increasing trend of $\Delta HCHO/\Delta CO$ from 20 ppt/ppb to over 30 ppt/ppb with limited data and simulated a flat trend of $\Delta HCHO/\Delta CO$ within 1 h age since emission from a Savanna fire plume in Africa. Müller et al. (2016) also observed an increasing trend of $\Delta HCHO/\Delta CO$ with an average of 22.7 ppt/ppb and simulated a flat or slightly decreasing trend of $\Delta HCHO/\Delta CO$ in a small fresh agricultural biomass burning plume in Georgia, US. While such case studies are valuable, we lack a general understanding of the drivers of plume trends and plume-to-plume variability in HCHO evolution.

HCHO is also one of the few VOCs that can be observed from space, and the global coverage of satellite observations has been leveraged to provide insights into a variety of atmospheric chemistry questions. HCHO is correlated with organic aerosols in biomass burning air masses, and this correlation might be exploited to estimate organic aerosol abundance from satellite HCHO measurements (Liao et al., 2019). In regions with constant or very high OH reactivity, HCHO variability is closely linked to OH variability (Valin et al., 2016; Wolfe et al., 2019) and may be used to infer OH. Satellite HCHO columns have also been widely used to constrain emissions of isoprene and other VOCs (Fu et

81 al., 2007; Kaiser et al., 2018; Marais et al., 2014; Millet et al., 2008; Stavrakou et al., 2009). Understanding the
82 emissions, chemistry and trends of HCHO in wildfires will facilitate the application of satellite HCHO towards broad-
83 scale wildfire smoke processes and impacts.
84
85 The Fire Influence on Regional to Global Environments and Air Quality experiment (FIREX-AQ) deployed a
86 comprehensive suite of instruments aboard the NASA DC-8 aircraft to study wildfires and agricultural fires in the US.
87 It provided a great opportunity to systematically study the emissions and chemistry of HCHO in wildfire plumes. In
88 the following, we describe the HCHO dependence on plume age in wildfire plumes from FIREX-AQ, assess the
89 drivers of HCHO trends, and examine the factors controlling variability in secondary HCHO production.
90

91 **2. Methods**

92 **2.1 FIREX-AQ field campaign and measurements description**

93 During FIREX-AQ, a combination of four aircraft (the NASA DC-8, NASA ER-2, and two NOAA Twin Otters)
94 with a comprehensive suite of in situ and remote sensing instruments were deployed to characterize fire emissions
95 and chemistry with operational bases in Boise, ID and Salina, KS from July to September 2019. This study focuses
96 on wildfire plumes sampled by the NASA DC-8 aircraft during FIREX-AQ.
97

98 In situ HCHO observations were acquired by several instruments onboard the DC-8; here we primarily use
99 measurements from the In Situ Airborne Formaldehyde (ISAF) instrument (Cazorla et al., 2015). ISAF uses laser-
100 induced fluorescence to detect HCHO. A tunable UV laser excites HCHO molecules to an excited electronic state and
101 the resulting fluorescence is detected with a photon-counting photomultiplier tube. The laser wavelength is modulated
102 on and off a rotational absorption feature (353.163 nm), and the difference between the "online" and "offline" signals
103 is proportional to the HCHO concentration.
104

105 ISAF was calibrated pre- and post-mission with a compressed-gas HCHO cylinder (584 ± 15 ppbv in nitrogen, Air
106 Liquide). Sensitivity typically varies by less than 5% between calibrations. Flow meters for the standard dilution
107 system were calibrated against a DryCal calibrator (Mesa Labs) with an accuracy of > 99%. The HCHO standard
108 concentration was calibrated before and after the field deployment with an MKS Multigas 2031 Fourier transform
109 infrared spectrometer. Gas standard mixing ratios are typically reproducible to within 2% of the mean value measured
110 over multiple years. IR-determined mixing ratios are adjusted by a factor of 0.96 based on a separate long-path UV
111 absorption experiment (Cazorla et al., 2015). Thus, ISAF HCHO mixing ratios are ultimately tied to the UV cross
112 sections of Meller and Moortgat (2000) as recommended by the JPL 2011 evaluation (Sander et al., 2011). The
113 detection limit of ISAF was 30 pptv for 1-Hz data at signal/noise = 1 and the accuracy of ISAF HCHO measurements
114 was estimated as 10% + 10 pptv. The $1/e$ response time of ISAF during FIREX-AQ was about 300 ms, limited mainly
115 by flow through the sample cell.
116

During FIREX-AQ, ISAF HCHO measurements correlated with those from the Compact Atmospheric Multispecies Spectrometer (CAMS) (Richter et al., 2015), with a coefficient of determination r^2 of 0.99, a slope of 1.27 (CAMS vs. ISAF), and a near-zero intercept for 1-Hz average wildfire data from equally weighted orthogonal distance regression (Fig. S1). The systematic bias between the CAMS and ISAF measurements exceeds the combined stated uncertainty (10% for ISAF, 6% for CAMS). Post-mission comparisons suggest this discrepancy is due to the absolute calibration of compressed-gas HCHO standards, which are tied to literature-recommended UV (ISAF) or IR (CAMS) cross sections; the source of this discrepancy is still under investigation. Remotely-sensed HCHO column retrievals rely on the same UV cross sections (De Smedt et al., 2018) that are used to calibrate the ISAF instrument. The HCHO enhancements in the plumes (Sect 3.1) and the estimated effective yield of HCHO from VOC oxidation by OH (Sect. 3.3) can have a potential low bias of 27% due to the ISAF and CAMS HCHO measurement difference. This uncertainty proportionally affects quantitative analysis results but does not alter qualitative conclusions.

We also use several supporting measurements in our analysis. CO was measured via mid-IR wavelength modulation spectroscopy by the Differential Absorption Carbon Monoxide Measurement (DACOM) instrument (Sachse et al., 1991). Photolysis rates were derived from the Actinic flux measurements by the Charged-coupled device Actinic Flux Spectroradiometer (CAFS) (Hall et al., 2018). Alkenes were measured by the NOAA Whole Air Sampler (iWAS) (Lerner et al., 2017). Ozone (O_3) measurements were from the NOAA Chemiluminescence instrument (Bourgeois et al., 2020). OH reactivity calculations used VOCs measurements from the NOAA Proton-Transfer Reaction Time-of-Flight Mass Spectrometry (PTR-ToF-MS) (Yuan et al., 2016), NCAR Trace Organic Gas Analyzer (TOGA) (Apel et al., 2015) outfitted with a Time-of-Flight Mass Spectrometer, NOAA Airborne Cavity Enhanced Spectrometer (ACES) (Min et al., 2016), and NOAA Iodide Ion Time-of-Flight (ToF) Chemical Ionization Mass Spectrometer (CIMS) (Veres et al., 2020), listed in Table S1. Our analysis uses in situ measurements that are merged to the iWAS sampling period, which ranged from 1-9 seconds per canister, such that multiple samples were often acquired within a single plume crossing.

2.2 Normalized excess mixing ratio (NEMR) and physical age definitions

NEMR is defined as the difference between the concentration of species X in the plume and in the background air outside of the plume, normalized by the difference between CO concentrations in the plume and the background outside of the plume. Because photochemical production of CO is very small compared to the high CO concentrations in the biomass burning plumes (e.g., CO production from HCHO photolysis and oxidation for 1 h is about 2.5 ppbv, which is < 1% of CO concentrations of 985 ppbv on average in the plumes), trace gases concentrations are normalized to CO in the biomass burning plumes to account for dilution, as in many previous biomass burning studies (e.g., Müller et al., 2016; Selimovic et al., 2019).

$$\text{NEMR} = \frac{\Delta X}{\Delta CO} \tag{1}$$

151 The background air outside of the plumes was manually selected and could be different or the same for different
152 transects of the same plume, depending on the availability of the iWAS data. The HCHO NEMR is denoted by nHCHO
153 below.
154
155 Physical age was estimated using a Lagrangian trajectory analysis (Holmes et al., in preparation) and described briefly
156 here. Fire source locations were pinpointed using the MODIS/ASTER Airborne Simulator (MASTER) instrument
157 data onboard the DC-8. Upwind trajectories from aircraft locations were computed and the advection age was
158 calculated from the time when a trajectory was closest to the fire. Plume rise time from the surface to the trajectory
159 initialization altitude assumed a vertical wind speed of 7 m/s. The smoke age is the sum of advection age plus rise age
160 averaged over several meteorological models. The average uncertainty of the estimated physical age for the analyzed
161 wildfire plumes was 37% with an interquartile range of 20% based on the range of ages derived from the High-
162 Resolution Rapid Refresh (HRRR), North American Mesoscale Forecast System (NAM) CONUS Nest, and Global
163 Forecast System (GFS 0.25°) meteorological datasets.
164

165 **2.3 Plume selection**

166 Details about the specific selected wildfire plumes among all sampled wildfire plumes during FIREX-AQ are provided
167 in Table S2. Wildfire plumes that meet the conditions listed below are above the background HCHO concentrations,
168 which typically vary from 100 ppt – 1 ppb during FIREX-AQ, and are selected to study the evolution of HCHO in
169 wildfires.
170 a) Lagrangian sampling pattern
171 Lagrangian sampling patterns are defined as flight tracks intercepted the plumes with flight leg directions
172 approximately perpendicular to the horizontal wind directions and more than three transects downwind with different
173 distances from the fire.
174 b) Appropriate VOC decay for the period analyzed with sufficient data samples
175 We selected the plume samples where chemical age correlated with physical age. This was defined by a coefficient of
176 determination $r^2 \geq 0.57$ for a plot of ln(trans-2-butene/propene) or ln(cis-2-butene/propene) vs physical age. We used
177 2-butenes/propene as chemical age tracers in this analysis because these gases have comparable lifetimes to physical
178 age for most of the analyzed plumes. We filtered out plume data if the correlation coefficient of ln(trans-2-
179 butene/propene) or ln(cis-2-butene/propene) vs. physical age degraded at older physical ages. Figure S2 shows
180 ln(trans-2-butene/propene) and ln(cis-2-butene/propene) vs. physical age for the plumes that satisfied conditions a)
181 and had iWAS data available. The threshold of $r^2 = 0.57$ is chosen by visual inspection of all VOC decay in Fig. S2.
182 We also filtered out plumes with total number of data points < 8 in the iWAS sample periods for an entire selected
183 circuit of multiple plume transects with good VOC decay. Due to the inhomogeneity of the plumes, too few data points
184 can introduce large bias. In the analyzed plume periods, ln(trans-2-butene/propene) or ln(cis-2-butene/propene) also
185 has good correlations with the maleic anhydride/furan ratio (Fig. S3), another tracer of chemical age in biomass
186 burning plumes (Coggon et al., 2019; personal communication with Carsten Warneke and Matthew M. Coggon, 2021).

187   The Mica and Lick Creek plume on 02 August 2019 is the plume with the least number of data points among the

188   selected plumes (N = 8).

189

190   The above filters, applied to a total of 26 fire plumes, yield 11 daytime plumes and 1 nighttime plume that are

191   suitable for our analysis (Table S2). The nighttime plume on 12 August was after 8:00 pm local time with average

192   O_3 photolysis rate of essentially zero. One of the twelve plumes (Blackwater) occurred in the southeast US and the

193   remaining 11 plumes were in the western US.

194

195   **2.4 Estimating average OH concentrations in the plumes**

196   Plume photochemical age is estimated based on the relative decay of primary emitted VOCs that have different

197   reaction rate coefficients with OH (e.g., Warneke et al., 2007). We can estimate the average concentration of OH by

198   combining the photochemical age with the trajectory-based air mass age. Cis-2-butene/propene ratios and trans-2-

199   butene/propene ratios are used to estimate OH in this analysis because these gases have lifetimes comparable to

200   physical age (2–6 h) for most of the analyzed plumes and using two VOC ratios help reduce the uncertainty. The

201   lifetimes of propene, cis-2-butene, and trans-2-butene are approximately 4.5 h, 2.3 h, and 1.8 h, respectively, at OH

202   concentrations of 2×10^6 molecules cm^{-3} (Atkinson et al., 2006). Because both 2-butenes also differ from propene in

203   O_3 reaction rate coefficients, the reactions of these alkenes with O_3 are also considered when we estimate the OH

204   concentrations. We assume that the variability in the butenes–propene relationship is driven by OH and O_3 and that

205   there is negligible change in the relative emission ratios over the sampled plumes. Different slopes in cis-2-

206   butene/propene and trans-2-butene/propene vs plume age (Fig. S2) depend on the differences in reaction rate

207   coefficients of OH and O_3 with 2-butene (cis-2-butene and trans-2-butene) and propene, in addition to OH and O_3

208   concentrations, as shown in Eq. (2). These reaction rate coefficients are those reported by Atkinson et al. (2006) with

209   real time temperature and pressure dependence. The plumes average reaction rate coefficients are $k_{propene\_OH}$ =

210   3.1×10^{-11} cm^3 molecule^{-1}s^{-1}, $k_{cis-2-butene\_OH}$ = 6.4×10^{-11} cm^3 molecule^{-1}s^{-1}, $k_{trans-2-butene\_OH}$ = 8.0×10^{-11} cm^3

211   molecule^{-1}s^{-1}, $k_{propene\_O_3}$ = 6.4×10^{-18} cm^3 molecule^{-1}s^{-1}, $k_{cis-2-butene\_O_3}$ = 9.9×10^{-17} cm^3 molecule^{-1}s^{-1}, and

212    $k_{trans-2-butene\_O_3}$ = 1.5×10^{-16} cm^3 molecule^{-1}s^{-1}.

213    $\ln \frac{butene}{propene} = \ln \frac{butene_0}{propene_0} - \{(k_{butene+OH} - k_{propene+OH})[OH] + (k_{butene+O_3} - k_{propene+O_3})[O_3]\}t$

214   (2)

215   OH concentrations are derived from the slope of $\ln \frac{butene}{propene}$ vs. t (physical age), the measured ozone concentrations

216   and the reaction rate coefficients.

217    $[OH] = \frac{slope_{butene} + (k_{butene+O_3} - k_{propene+O_3})[O_3]}{k_{propene+OH} - k_{butene+OH}}$ (3)

218   Because the instantaneous O_3 measurements do not reflect the oxidation history, the average ozone concentration of

219   the entire circuit with multiple transects is used to represent the integrated O_3 effect on alkene oxidation. The

220   uncertainty due to O_3 variation and the uncertainty in the slope of $\ln \frac{butene}{propene}$ vs. t are propagated to estimate the total

221 uncertainty in plume-average OH. Butene in Eq. (2) and (3) represents trans-2-butene or cis-2-butene, both of which
222 are used in average OH estimation. O_3 variation, uncertainty in OH due to O_3 variation, total OH uncertainty, and
223 estimated OH are listed in Table S3.

224

225 **2.5 Calculating primary HCHO normalized mixing ratios and secondary HCHO production rates**

226 To understand the relative importance of primary emission vs. secondary production of HCHO in fire plumes
227 downwind, we calculate primary and secondary HCHO as the plume ages. The primary HCHO time profile is
228 calculated by the following equation:

229 $\text{nHCHO}_{primary} = \text{nHCHO}_0 \exp(-(J_{HCHO} + k_{HCHO}[\text{OH}])t)$ (4)

230 where nHCHO_0 is equal to the fitted observed nHCHO (HCHO NEMR) closest to the fire source, J_{HCHO} is the measured
231 HCHO photolysis frequency in iWAS sample periods averaged and interpreted in physical age space, k_{HCHO} is the
232 reaction rate coefficient between HCHO and OH, and t is the physical age. $\text{nHCHO}_{secondary}$ is calculated by subtracting
233 $\text{nHCHO}_{primary}$ from the measured nHCHO. Here we assumed the fitted observed nHCHO closest to the fire source is
234 equal to nHCHO at the emission source. This assumption will not impact the secondary nHCHO production rate
235 calculated below.

236

237 To characterize secondary HCHO production in wildfire plumes, we calculate the secondary nHCHO production rate.
238 The secondary nHCHO production rate is derived from the HCHO mass balance equation.

239 $\frac{d\ \text{HCHO}}{dt} = P - L - D$ (5)

240 where P is chemical production, L is chemical loss, and D is dilution. The calculation of the secondary nHCHO
241 production rate is shown in Eq. (6). The derivation of Eq. (6) from Eq. (5) can be found in Appendix A.

242 $\frac{P}{\Delta CO}$ (or P_{nHCHO}) $= \frac{dnHCHO}{dt} + (J_{HCHO} + k_{HCHO}[OH])nHCHO.$ (6)

243 Here, $\frac{d\ \text{nHCHO}}{dt}$ is taken as the slope of measured nHCHO vs physical age and other parameters are as defined above.

244

245 **2.6 Impact of potential variation in HCHO emission ratios on nHCHO trend**

246 In this analysis, we assume the variability in the HCHO/CO emission ratio (that is, nHCHO at the source) is much
247 smaller than the variability in nHCHO induced by chemistry for any single fire plume. Emission factors of both HCHO
248 and CO (that is, g of gas per kg of fuel burned) depend on MCE, fuel type, and other factors (e.g., Liu et al., 2017;
249 Yokelson et al., 1999). Normalizing HCHO by CO removes the strong negative dependence of HCHO emission factors
250 on MCE. A small positive trend of nHCHO vs. MCE is due to higher nHCHO and MCE for the eastern US wildfire
251 plume than the western US wildfire plumes (Fig. S4). No clear trend of MCE in nHCHO plume evolution was observed
252 in FIREX-AQ data (Fig. S5). Emissions of CO_2 correlate with fire radiative power (FRP) detected by satellite during
253 FIREX-AQ, and the variability of FRP could affect the variability of downwind concentrations (Wiggins et al., 2020).
254 We found that HCHO correlates with CO_2 (Fig. S6a) and thus likely also with FRP because the change of measured

255   CO_2 correlates with the change of FRP (Wiggins et al., 2020). To account for emission variation and dilution, which

256   are main factors affecting the absolution concentrations of trace gases and aerosols in the plumes, HCHO is normalized

257   to CO to investigate the impact of photochemistry on HCHO evolution in the plumes. Photochemistry takes place

258   while emission varies. When normalized to CO, nHCHO does not strongly depend on CO_2 (Fig. S6b and Fig. S7) or

259   FRP. FRP and MCE do not control the trends of nHCHO.

260

2.7 OH reactivity calculation

262   We calculate the observed OH reactivity using the Framework for 0-D Atmospheric Modeling (F0AM v4) (Wolfe et

263   al., 2016) with the Master Chemical Mechanism v3.3.1 (MCM; Jenkin et al., 2015) and additional chemical reactions

264   from recent publications of newly-observed biomass burning species and reactions (Coggon et al., 2019; Decker et al.,

265   2019). The VOC chemical species included in the F0AM model are listed in Table S1. We calculate the OH-VOC

266   reactivity ($\sum k_i VOC_i$) by excluding OH reactions with NO_2 and CO from the total OH reactivity and define the

267   normalized OH-VOC reactivity or normalized total OH reactivity as OH-VOC reactivity normalized by CO or total

268   OH reactivity normalized by CO.

269

3. Results and discussion

3.1 OH concentration estimation

272   OH is the main oxidant that reacts with VOCs to produce HCHO in the daytime. As described in Sect. 2.4, we estimate

273   plume-average OH concentrations using the relative decays of 2-butenes to propene via Eq. (3). The decay of the

274   natural logarithm of the trans-2-butene to propene ratio and the cis-2-butene to propene ratio with physical age is

275   plotted in Fig. S2. Figure S2 includes all the plumes that meet selection condition (a) in Sect.2.3, 12 plumes of which

276   with good correlations ($r^2 = 0.57$–0.99) between 2-butenes/propene and plume age and sufficient data (data points >

277   8) are selected for this analysis. The lowest correlation coefficient of the selected plumes occurs for the nighttime

278   plume on 12 August 2019 and the daytime plume on 29 July 2019. This indicates that the photochemical age of these

279   plumes is consistent with their physical age, and the oxidation chemistry can be reasonably represented by average

280   OH and O_3. The slopes in Fig. S2 infer the estimated OH concentrations and their coefficients of determination (r^2)

281   imply how good the VOC decay can be used to estimate OH.

282

283   The estimated average OH concentrations for the 12 plumes are shown in Fig. 1. The uncertainties in OH

284   concentrations are based on the standard error in the slope of ln(butenes/propene) vs physical age and the standard

285   deviation of O_3 concentrations. The average and standard deviation of O_3 concentrations and the uncertainty in OH

286   estimation due to the impact of O_3 standard deviation are listed in Table S3. Plume-to-plume variability in average

287   OH concentrations is generally consistent between the two ratio methods. OH concentrations from trans-2-butene

288   are systematically higher than those from cis-2-butene by 27% on average, which may reflect systematic bias in

289 reaction rate coefficients or observations. For all plumes where both calculations were available, differences are
290 within the combined uncertainties. The average OH concentrations from trans-2-butene to propene and cis-2-butene
291 to propene were used to represent the average OH concentrations of the plumes. The average OH concentrations
292 covered a large range, varying from $-0.5(\pm 0.5)\times 10^6$ (for a nighttime plume) to $5.3(\pm 0.7)\times 10^6$ molecules cm^{-3}.

293

294 **3.2 Trends of HCHO in wildfire plumes**

295 nHCHO in wildfire plumes can increase or decrease as plumes age. The trends of measured nHCHO vs. physical age
296 and the corresponding quadratic polynomial regression for 12 selected plumes are plotted in Fig. 2. Quadratic
297 polynomial regression is used because it has suitable degrees of freedom to capture the trends. Considering the CO
298 measurement uncertainty of $\leq 7\%$ and HCHO measurement uncertainty of 10%, the uncertainty of nHCHO is
299 estimated to be $\pm 12\%$ with a potential systematic low bias of as much as 27% (based on the difference between ISAF
300 and CAMS). Random error due to HCHO and CO measurement precision is negligible when averaging over the iWAS
301 integration time in high-concentration biomass burning plumes.

302

303 In the absence of secondary production, we expect nHCHO to decay with a time constant of a few hours in the daytime.
304 The blue curves in Fig. 2 show the predicted decay of initial nHCHO using observed HCHO photolysis rates and
305 measurement-derived OH concentrations. Because the variability in nHCHO in one transect is significant, we use the
306 start point of the observed nHCHO fitted curve to represent the observed nHCHO closest to fire. HCHO photolysis
307 frequencies are averaged generally over each transect and linearly interpolated to determine continuous age-dependent
308 photolysis frequencies. The calculated nHCHO without production is higher than primary (emitted) nHCHO because
309 some HCHO production and loss had already occurred before the closest transect.

310

311 The fraction of primary and secondary nHCHO varies from plume to plume and depends on secondary HCHO
312 production rates and total HCHO loss rates. This can be inferred from nHCHO trends and the loss-only nHCHO
313 decays in Fig. 2 and is also shown in Fig. S8. We estimate the fraction of primary HCHO by assuming nHCHO and
314 the loss rate of nHCHO are constant between emission and the closest observation. The primary HCHO fraction could
315 decay rapidly to be 60% in about 1 h of aging or it could decay slowly to still account for 60% in about 5h of aging.
316 The primary and secondary fractions of HCHO indicate the impact of direct emission and photochemistry on the fire
317 plume composition downwind. The slowing down increase in secondary nHCHO fraction with time probably indicate
318 that the production of secondary nHCHO slows down with physical age. The average and standard deviation of
319 nHCHO production and loss rates for each plume are provided in Table S4.

320

321 HCHO production exceeds loss in 9 of the 12 selected plumes, indicated by overall positive trends of nHCHO vs.
322 physical age in Fig. 2. Plumes exhibiting overall negative nHCHO trends (20190725 Shady 2, 20190803 Williams
323 Flats 1 and 20190806 Williams Flats) have higher overall nHCHO loss rates than production rates (Table S4). This
324 shows that fire-to-fire variability in the overall nHCHO trend relates to the balance between loss (via photolysis) and

325 production (via VOC oxidation). HCHO loss by photolysis can be either higher or lower than the loss by reaction with
326 OH, but on average photolysis is faster. HCHO loss via photolysis accounts for $63 \pm 27\%$ of the total HCHO loss in
327 daytime plumes. The average HCHO lifetime by photolysis was $8.2 (\pm 8.8)$ h for the 11 daytime plumes, shorter than
328 the average HCHO lifetime by OH oxidation of $23.5 (\pm 31.3)$ h. For some plume transects, there was significant
329 variability in HCHO photolysis frequencies over iWAS averaging intervals due to the aerosol radiative effects.
330 Applying filters to only analyze the data with relatively homogeneous in-plume HCHO photolysis rates does not alter
331 our conclusions. Plume-average OH is not well correlated with the HCHO photolysis frequency (Fig. S9), likely due
332 to inter-fire variability of OH sources and sinks.
333
334 Besides the variability among different plumes, nHCHO production and loss also vary within a plume across physical
335 age. In all analyzed plumes, nHCHO slope shifts from positive to neutral or negative within the first 2-6 h (Fig. 2).
336 Figure S10 shows the age progression of nHCHO production, loss, and net change for the 12 plumes. In general, both
337 production and loss decrease with age. Decreases in both are expected due to declining solar radiation, which results
338 from the typical late-afternoon FIREX-AQ sampling strategy. Reduced production with increasing age may also
339 reflect the decay of reactive VOC and oxidant precursors (e.g., HONO).
340

341 **3.3 Controls on secondary HCHO formation**

342 The secondary HCHO production rate is determined by a mass balance approach with loss, production, and dilution
343 terms, as discussed in Sect. 2.5. The average secondary nHCHO production rate correlates with the average OH
344 concentration ($r^2 = 0.69$, Fig. 3a). The secondary production rates of nHCHO were calculated from the trends of
345 observed nHCHO ($\frac{dnHCHO}{dt}$), photolysis loss rate and OH (Eq. 6). Although OH concentrations are used to calculate
346 secondary nHCHO production rates, the nHCHO loss term (k[OH]nHCHO) due to OH only accounts for $2-35\%$ of
347 all the terms on the righthand side of Eq. (6), which is used to calculate secondary nHCHO production rate for the
348 plumes. This indicates that the good correlation between secondary nHCHO production rate and OH is not due to the
349 inclusion of OH in nHCHO production rate calculation. The uncertainty in nHCHO secondary production rates for
350 each plume is estimated from the standard deviation of the calculated nHCHO secondary production rates along the
351 physical age of the plume. The uncertainty in estimated OH is determined by the propagated uncertainties of OH from
352 trans-2-butene to propene ratios and cis-2-butene to propene ratios. The nHCHO secondary production rates also
353 correlate with the HCHO photolysis ($r^2 = 0.53$ uncertainty weighted linear regression), which is not unexpected as OH
354 and J$_{HCHO}$ positively correlate as well. The correlation between nHCHO secondary production rates with oxidant ozone
355 is poor ($r^2 = 0.1$ from bivariate regression). The good correlations ($r^2 = 0.69$) between the secondary production rate
356 of nHCHO and average OH indicate that the variability in OH is a key driver of the secondary production rate of
357 nHCHO. Although there is only one eastern US wildfire plume sampled during FIREX-AQ, it has high VOCs,
358 nHCHO, nHCHO production rate, and OH, and the inclusion of the eastern US wildfire increase the coefficient of
359 determination (r^2 from 0.54 to 0.69) and the slope (m from 0.30 to 0.33) of nHCHO secondary production rates vs.
360 OH. More wildfire sampling is needed to understand the difference between western and eastern US wildfires.

364

365 Figure 3a is color-coded with normalized OH-VOC reactivity calculated from measured VOCs (Sect. 2.7). Plume-

366 average normalized OH-VOC reactivity ranges from 11 to 31 s^{-1} (ppm CO)$^{-1}$, which is about 20% lower than

367 normalized total OH reactivity across the analyzed plumes. nHCHO production rates vs. normalized OH-VOC

368 reactivity (Fig. S11a) shows a lower coefficient of determination (r^2) and a higher p value than Fig.3a. Because

369 uncertainty weighted linear regression yields a low r^2= 0.08 for Fig. S11a, unweighted (or equally weighted) bivariate

370 linear regression is used. P-values in Fig. 3 show the correlation between nHCHO production rate vs. OH ($p = 0.004$)

371 or vs. OH× normalized OH-VOC reactivity ($p = 0.003$) is statistically significant ($p < 0.05$). Because the yield of

372 HCHO from VOC oxidation is calculated in the study, normalized OH-VOC reactivity instead of normalized total OH

373 reactivity is mainly used. A plot of nHCHO production rate vs. normalized total OH reactivity color coded with OH

374 is shown in Fig. S11b. Similar to Fig. S11a, the correlation between nHCHO production rate with normalized total

375 OH reactivity is also not significant. Because nHCHO trend, OH concentration, and normalized OH-VOC reactivity

376 all depend on physical age, in addition to the different properties of the plumes, the difference in physical age among

377 these plumes also has an impact on the average values.

378

379 Figure 3b shows nHCHO production vs. the product of OH and dilution-normalized observed OH-VOC reactivity

380 (averaged for each plume). The latter is a lower limit for the total average OH loss/production rate as observations do

381 not include all OH sinks. The correlation is slightly higher than that in Fig. 3a because variability in normalized OH-

382 VOC reactivity plays a smaller role than OH in affecting P_{nHCHO}. The slope of this relationship, 0.33 ± 0.05, is a metric

383 for the effective yield of HCHO from OH-initiated VOC oxidation. Assuming that reaction of OH with a VOC is the

384 rate-limiting step and ignoring non-OH sources, integrated HCHO production can be written as in Eq. (7).

385 $$P_{HCHO} = \sum \alpha_i k_i [OH][X_i] = \alpha_{eff} k'_{OH}[OH] \qquad (7)$$

386 Where α_i is the yield of HCHO from OH oxidation of any VOC reactant X_i and depends on both the structure of X

387 and the fate of reactive intermediates like peroxy radicals, k_i is the reaction rate coefficient for VOC$_i$ + OH, k'_{OH}

388 represents OH-VOC reactivity, and α_{eff} is the effective yield weighted over OH-VOC reactions. If all OH reactivity

389 (including reactions with CO and NO$_2$) instead of OH-VOC reactivity is considered, α_{eff} will be about 20% smaller.

390 As discussed by Valin et al. (2016), α_{eff} from all OH reactivity is expected to range from 0.2 to 0.4 depending on the

391 magnitude of NO$_x$ and the magnitude and speciation of VOC. The yield reported here (0.28 for all OH reactivity) is

392 on the low end of this range, implying that HCHO production in the plumes is not very efficient due to the nature of

393 the emitted VOC and/or the balance of RO$_2$ reactions with NO, HO$_2$, and other RO$_2$. High α_{eff} values reported by

394 Valin et al. (2016) occur in high isoprene emission regions, implying the emitted VOCs in wildfires are not as

395 efficient as isoprene in producing HCHO. Our α_{eff} of 0.28, when considering all OH reactivity, is higher than the

396 value of 0.20 (± 0.01) derived by Wolfe et al. (2019) for total-column HCHO in the remote troposphere, where

397 methane oxidation is the primary HCHO source. The potential low bias in observed HCHO could lead to a

398 proportional (27%) low bias in α_{eff}. Species that are highly reactive and present in large quantities such as CH$_3$CHO

399 are important for OH-VOC reactivity and α_{eff} calculation. We use PTRMS CH$_3$CHO data in OH-VOC reactivity

Deleted: does not

Deleted: meaningful fit

Formatted: Superscript

402 calculation because they are more easily integrated over the iWAS sampling time than TOGA CH_3CHO. This
403 indicates that besides the potential missing VOCs, the uncertainties in measured VOCs concentrations and different
404 sampling time resolutions can also contribute to the uncertainties in OH reactivity and α_{eff}. The α_{eff} for the one
405 eastern US wildfire plume is higher than that of the western US wildfire plumes but more sampling of eastern
406 wildfire plumes is needed to determine if there is a statistical difference in α_{eff}. Higher NO_x/VOC ratio in the eastern
407 than western US wildfire plumes may contribute to the higher α_{eff} because more NO_x generally means more radical
408 turnover and a larger fraction of $RO_2 + NO$, both of which favor HCHO production.

409

410 **3.4 Implications for interpretation of satellite observations**

411 The quantification of the evolution of HCHO in wildfire plumes can be leveraged to enhance interpretations of satellite
412 remote sensing observations. The good correlation of dilution-corrected secondary HCHO production and oxidant
413 levels suggests the use of satellite HCHO data to estimate oxidant levels in biomass burning plumes. Similar to the
414 studies of NO_2 lifetime from satellite NO_2 data (e.g., Laughner and Cohen, 2019; Liu et al., 2016), with parameterized
415 production rates of HCHO as a function of OH from this study, the effective lifetime of HCHO and OH concentrations
416 in the wildfire plumes could potentially be derived from remote sensing HCHO and CO data if the photolysis rates
417 can be properly parameterized. Satellite HCHO retrievals in biomass burning plumes remain challenging, and
418 information about vertical distributions of trace gases and aerosols from airborne measurements are likely needed to
419 improve satellite retrievals in biomass burning plumes. The effective yield of HCHO from this analysis indicates that
420 the biomass burning VOCs could be less efficient than isoprene in producing HCHO, although other factors such as
421 balance of RO_2 reactions with NO, HO_2, and other RO_2 can play a role. This information may be useful for estimating
422 VOC emissions from satellite HCHO data.

423

424 **4. Conclusions**

425 We studied the chemical evolution of HCHO in wildfire plumes during FIREX-AQ. Twelve well-developed plumes
426 with consistent chemical and physical age 1–6 h downwind were selected among 26 wildfire plumes sampled. During
427 plume transport and aging, dilution-corrected HCHO increased in smoke from nine wildfires and decreased in three,
428 depending on the balance of HCHO production and loss processes. Secondary nHCHO production tracks average OH
429 concentrations, indicating that the variability in OH rather than the variability in the reactive VOC pool drives the
430 production of nHCHO in these wildfire plumes. The effective HCHO yield from OH-initiated VOC oxidation is
431 estimated to be 0.33 (± 0.05), which is about in the middle of previous studies of isoprene-rich, urban VOC-dominated
432 and remote atmospheric background regions.

Appendix A. Derivation of secondary nHCHO production rate from mass balance equation

Change of HCHO concentration with time can be obtained from mass balance equation (Eq. A1)

$$\frac{d\,HCHO}{dt} = P - L - D \qquad\qquad (A1)$$

where P is the HCHO chemical production term; L is the HCHO chemical loss term; and D is the dilution term.

Considering the HCHO normalized excess mixing ratio ($nHCHO = \frac{HCHO - HCHO_{bkg}}{CO - CO_{bkg}}$) and assuming that the HCHO

background change is relatively small ($\frac{d\,HCHO\,bkg}{dt} \approx 0$), $\frac{d\,HCHO}{dt}$ can be written as

$$\frac{d\,HCHO}{dt} = \Delta CO\frac{d\,nHCHO}{dt} + nHCHO\frac{d\,\Delta CO}{dt}. \qquad\qquad (A2)$$

Because L, D and P terms are as

$$L = (J_{HCHO} + k_{HCHO}[OH])HCHO. \qquad\qquad (A3)$$

$$D = -k_{dil}(HCHO - HCHO_{bkg}) = -\frac{1}{\Delta CO}\frac{d\,\Delta CO}{dt}HCHO. $$

$$\qquad\qquad (A4)$$

$$P = \frac{d\,HCHO}{dt} + L + D = \Delta CO\frac{d\,nHCHO}{dt} + nHCHO\frac{d\,\Delta CO}{dt} + (J_{HCHO} + k_{HCHO}[OH])HCHO - \frac{1}{\Delta CO}\frac{d\,\Delta CO}{dt}HCHO.$$

$$\qquad\qquad (A5)$$

By assuming HCHO >> HCHO$_{bkg}$, $\frac{P}{\Delta CO}$ can be written as

$$\frac{P}{\Delta CO} = \frac{dnHCHO}{dt} + (J_{HCHO} + k_{HCHO}[OH])nHCHO. \qquad\qquad (A6)$$

Where $\frac{d\,nHCHO}{dt}$ can be derived from measured HCHO and CO vs physical age; J_{HCHO} is the HCHO photolysis coefficient, derived from in-situ actinic flux measurements; OH is calculated from VOCs ratios (Sect.2.4); k_{HCHO} is the reaction rate coefficient of HCHO and OH.

Data and code availability:

Data are publicly available at https://www-air.larc.nasa.gov/missions/firex-aq/index.html with a dataset doi: FIREX-AQ DOI: 10.5067/SUBORBITAL/FIREXAQ2019/DATA001. F0AM is available at https://github.com/AirChem/F0AM. Model setup scripts for this study are available from the contact author upon request.

Author contribution:

GMW and TFH directed the research direction. JL analyzed the data and discussed the results with GMW. JL wrote the manuscript. TFH, GMW, JMS, JL, and RAH made ISAF HCHO measurements. JBG, AL, and VS made iWAS measurements. GSD, JBN, HSH, JPG made DACOM CO measurements. SRH and KU made CAFS photolysis frequencies measurements. CDH, CHF, and AA provided the trajectories-based plume physical age. HSH provided MCE calculation. TBR, JP, and IB made O_3 measurements. CW, MMC, GIG, and KS made PTR-ToF-MS VOC

465   measurements. AF, DR, and PW made CAMS HCHO measurements. ECA and RSH made TOGA VOC

466   measurements. SSB, CCW, MAR, and RAW made ACES measurements. PRV and JAN made CIMS measurements.

467   All authors reviewed and commented on the manuscript.

468

469   **Acknowledgements:**

470   We gratefully acknowledge the crew, logistical personnel, science team and science leadership who facilitated the

471   FIREX-AQ mission. We also thank Gao Chen and Ali Aknan for the merged DC8 dataset used in this study. JL,

472   GMW, RAH, JMS, and TFH acknowledge support from the NASA Tropospheric Composition Program and NOAA

473   Climate Program Office's Atmospheric Chemistry, Carbon Cycle and Climate (AC4) program (NA17OAR4310004).

474   SRH and KU were funded by the NASA Tropospheric Composition Program (80NSSC18K0638). This material is

475   based upon work supported by the National Center for Atmospheric Research, which is a major facility sponsored by

476   the National Science Foundation under Cooperative Agreement No. 1852977. KS acknowledges the support from the

477   fund a Grant-in-Aid for Scientific Research (C) (18K05179) from the Ministry of Education, Culture, Sports, Science

478   and Technology of Japan.

479

480

481

482

References

Akagi, S. K., Yokelson, R. J., Wiedinmyer, C., Alvarado, M., Reid, J. S., Karl, T., Crounse, J. D., and Wennberg, P. O.: Emission Factors for Open and Domestic Biomass Burning for Use in Atmospheric Models, Atmos. Chem. Phys., 11, 4039-4072, doi:10.5194/acp-11-4039-2011, 2011.

Alvarado, L. M. A., Richter, A., Vrekoussis, M., Hilboll, A., Kalisz Hedegaard, A. B., Schneising, O., and Burrows, J. P.: Unexpected long-range transport of glyoxal and formaldehyde observed from the Copernicus Sentinel-5 Precursor satellite during the 2018 Canadian wildfires, Atmos. Chem. Phys., 20(4), 2057–2072, doi:10.5194/acp-20-2057-2020, 2020.

Alvarado, M. J., Logan, J. A., Mao, J., Apel, E., Riemer, D., Blake, D., Cohen, R. C., Min, K. E., Perring, A. E., Browne, E. C., Wooldridge, P. J., Diskin, G. S., Sachse, G. W., Fuelberg, H., Sessions, W. R., Harrigan, D. L., Huey, G., Liao, J., Case-Hanks, A., Jimenez, J. L., Cubison, M. J., Vay, S. A., Weinheimer, A. J., Knapp, D. J., Montzka, D. D., Flocke, F. M., Pollack, I. B., Wennberg, P. O., Kurten, A., Crounse, J., St. Clair, J. M., Wisthaler, A., Mikoviny, T., Yantosca, R. M., Carouge, C. C., and Le Sager, P.: Nitrogen oxides and PAN in plumes from boreal fires during ARCTAS-B and their impact on ozone: An integrated analysis of aircraft and satellite observations, Atmos. Chem. Phys., 10(20), 9739–9760, doi:10.5194/acp-10-9739-2010, 2010.

Apel, E. C., Hornbrook, R. S., Hills, A. J., Blake, N. J., Barth, M. C., Weinheimer, A., Cantrell, C., Rutledge, S. A., Basarab, B., Crawford, J., Diskin, G., Homeyer, C. R., Campos, T., Flocke, F., Fried, A., Blake, D. R., Brune, W., Pollack, I., Peischl, J., Ryerson, T., Wennberg, P. O., Crounse, J. D., Wisthaler, A., Mikoviny, T., Huey, G., Heikes, B., Sullivan, D. O., and Riemer, D. D.: J. Geophys. Res. Atmos., 120, 2505–2523, doi:10.1002/2014JD022121.Received, 2015.

Atkinson, R., Baulch, D. L., Cox, R. A., Crowley, J. N., Hampson, R. F., Hynes, R. G., Jenkin, M. E., Rossi, M. J., Troe, J., and IUPAC Subcommittee: Evaluated kinetic and photochemical data for atmospheric chemistry: Volume II – gas phase reactions of organic species, Atmos. Chem. Phys, 6, 3625–4055, doi:https://doi.org/10.5194/acp-6-3625-2006, 2006.

Bourgeois, I., Peischl, J., Thompson, C. R., Aikin, K. C., Campos, T., Clark, H., Commane, R., Daube, B., Diskin, G. W., Elkins, J. W., Gao, R. S., Gaudel, A., Hintsa, E. J., Johnson, B. J., Kivi, R., McKain, K., Moore, F. L., Parrish, D. D., Querel, R., Ray, E., Sánchez, R., Sweeney, C., Tarasick, D. W., Thompson, A. M., Thouret, V., Witte, J. C., Wofsy, S. C., and Ryerson, T. B.: Global-scale distribution of ozone in the remote troposphere from the ATom and HIPPO airborne field missions, Atmos. Chem. Phys., 20(17), 10611–10635, doi:10.5194/acp-20-10611-2020, 2020.

Cazorla, M., Wolfe, G. M., Bailey, S. A., Swanson, A. K., Arkinson, H. L., and Hanisco, T. F.: A new airborne laser-induced fluorescence instrument for in situ detection of formaldehyde throughout the troposphere and lower stratosphere, Atmos. Meas. Tech., 8(2), 541–552, doi:10.5194/amt-8-541-2015, 2015.

Coggon, M. M., Lim, C. Y., Koss, A. R., Sekimoto, K., Yuan, B., Gilman, J. B., Hagan, D. H., Selimovic, V., Zarzana, K. J., Brown, S. S., M Roberts, J., Müller, M., Yokelson, R., Wisthaler, A., Krechmer, J. E., Jimenez, J. L., Cappa, C., Kroll, J. H., de Gouw, J., and Warneke, C.: OH chemistry of non-methane organic gases (NMOGs) emitted from laboratory and ambient biomass burning smoke: Evaluating the influence of furans and oxygenated

520 aromatics on ozone and secondary NMOG formation, Atmos. Chem. Phys., 19(23), 14875–14899, doi:10.5194/acp-
521 19-14875-2019, 2019.

522 Decker, Z. C. J., Zarzana, K. J., Coggon, M., Min, K. E., Pollack, I., Ryerson, T. B., Peischl, J., Edwards, P., Dubé,
523 W. P., Markovic, M. Z., Roberts, J. M., Veres, P. R., Graus, M., Warneke, C., de Gouw, J., Hatch, L. E., Barsanti,
524 K. C., and Brown, S. S.: Nighttime Chemical Transformation in Biomass Burning Plumes: A Box Model Analysis
525 Initialized with Aircraft Observations, Environ. Sci. Technol., 53(5), 2529–2538, doi:10.1021/acs.est.8b05359,
526 2019.

527 Derek, Y.: Least-squares fitting of a straight line, Can. J. Phys., 46(16), 1845–1847, doi:10.1139/p68-523, 1968.

528 Fu, T. M., Jacob, D. J., Palmer, P. I., Chance, K., Wang, Y. X., Barletta, B., Blake, D. R., Stanton, J. C., and Pilling,
529 M. J.: Space-based formaldehyde measurements as constrains on volatile organic compound emissions in east and
530 south Asia and implications for ozone, J. Geophys. Res. Atmos., 112(6), 1–15, doi:10.1029/2006JD007853, 2007.

531 Garofalo, L. A., Pothier, M. A., Levin, E. J. T., Campos, T., Kreidenweis, S. M., and Farmer, D. K.: Emission and
532 Evolution of Submicron Organic Aerosol in Smoke from Wildfires in the Western United States, ACS Earth Space
533 Chem., 3(7), 1237–1247, doi:10.1021/acsearthspacechem.9b00125, 2019.

534 Gilman, J. B., Lerner, B. M., Kuster, W. C., Goldan, P. D., Warneke, C., Veres, P. R., Roberts, J. M., de Gouw, J.
535 A., Burling, I. R., and Yokelson, R. J.: Biomass burning emissions and potential air quality impacts of volatile
536 organic compounds and other trace gases from fuels common in the US, Atmos. Chem. Phys., 15(24), 13915–13938,
537 doi:10.5194/acp-15-13915-2015, 2015.

538 Hall, S. R., Ullmann, K., Prather, M. J., Flynn, C. M., Murray, L. T., Fiore, A. M., Correa, G., Strode, S. A.,
539 Steenrod, S. D., Lamarque, J. F., Guth, J., Josse, B., Flemming, J., Huijnen, V., Luke Abraham, N., and Archibald,
540 A. T.: Cloud impacts on photochemistry: Building a climatology of photolysis rates from the Atmospheric
541 Tomography mission, Atmos. Chem. Phys., 18(22), 16809–16828, doi:10.5194/acp-18-16809-2018, 2018.

542 Jaffe, D. A. and Wigder, N. L.: Ozone production from wildfires: A critical review, Atmos. Environ., 51, 1–10,
543 doi:10.1016/j.atmosenv.2011.11.063, 2012.

544 Jenkin, M. E., Young, J. C., and Rickard, A. R.: The MCM v3.3.1 degradation scheme for isoprene, Atmos. Chem.
545 Phys., 15(20), 11433–11459, doi:10.5194/acp-15-11433-2015, 2015.

546 Kaiser, J., Jacob, D. J., Zhu, L., Travis, K. R., Fisher, J. A., González Abad, G., Zhang, L., Zhang, X., Fried, A.,
547 Crounse, J. D., Clair, J. M. S., and Wisthaler, A.: High-resolution inversion of OMI formaldehyde columns to
548 quantify isoprene emission on ecosystem-relevant scales: Application to the southeast US, Atmos. Chem. Phys.,
549 18(8), 5483–5497, doi:10.5194/acp-18-5483-2018, 2018.

550 Koss, A. R., Sekimoto, K., Gilman, J. B., Selimovic, V., Coggon, M. M., Zarzana, K. J., Yuan, B., Lerner, B. M.,
551 Brown, S. S., Jimenez, J. L., Krechmer, J., Roberts, J. M., Warneke, C., Yokelson, R. J., and de Gouw, J.: Non-
552 methane organic gas emissions from biomass burning: Identification, quantification, and emission factors from PTR-
553 ToF during the FIREX 2016 laboratory experiment, Atmos. Chem. Phys., 18(5), 3299–3319, doi:10.5194/acp-18-
554 3299-2018, 2018.

555 Laughner, J. and Cohen, R. C.: Direct observation of changing NOx lifetime in North American cities, Science
556 366(6466), 723–727, 2019.

557   Lerner, B. M., Gilman, J. B., Aikin, K. C., Atlas, E. L., Goldan, P. D., Graus, M., Hendershot, R., Isaacman-

558   Vanwertz, G. A., Koss, A., Kuster, W. C., Lueb, R. A., Mclaughlin, R. J., Peischl, J., Sueper, D., Ryerson, T. B.,

559   Tokarek, T. W., Warneke, C., Yuan, B., and de Gouw, J. A.: An improved, automated whole air sampler and gas

560   chromatography mass spectrometry analysis system for volatile organic compounds in the atmosphere, Atmos.

561   Meas. Tech., 10(1), 291–313, doi:10.5194/amt-10-291-2017, 2017.

562   Liao, J., Hanisco, T. F., Wolfe, G. M., St. Clair, J., Jimenez, J. L., Campuzano-Jost, P., Nault, B. A., Fried, A.,

563   Marais, E. A., Gonzalez Abad, G., Chance, K., Jethva, H. T., Ryerson, T. B., Warneke, C., and Wisthaler, A.:

564   Towards a satellite formaldehyde - in situ hybrid estimate for organic aerosol abundance, Atmos. Chem. Phys., 19,

565   2765-2785, doi:10.5194/acp-2018-651, 2019.

566   Liu, F., Beirle, S., Zhang, Q., Dörner, S., He, K., and Wagner, T.: NOx lifetimes and emissions of cities and power

567   plants in polluted background estimated by satellite observations, Atmos. Chem. Phys., 16(8), 5283–5298,

568   doi:10.5194/acp-16-5283-2016, 2016.

569   Liu, X., Huey, L. G., Yokelson, R. J., Selimovic, V., Simpson, I. J., Müller, M., Jimenez, J. L., Campuzano-Jost, P.,

570   Beyersdorf, A. J., Blake, D. R., Butterfield, Z., Choi, Y., Crounse, J. D., Day, D. A., Diskin, G. S., Dubey, M. K.,

571   Fortner, E., Hanisco, T. F., Hu, W., King, L. E., Kleinman, L., Meinardi, S., Mikoviny, T., Onasch, T. B., Palm, B.

572   B., Peischl, J., Pollack, I. B., Ryerson, T. B., Sachse, G. W., Sedlacek, A. J., Shilling, J. E., Springston, S., St. Clair,

573   J. M., Tanner, D. J., Teng, A. P., Wennberg, P. O., Wisthaler, A., and Wolfe, G. M.: Airborne measurements of

574   western U.S. wildfire emissions: Comparison with prescribed burning and air quality implications, J. Geophys. Res.

575   Atmos., 122(11), 6108–6129, doi:10.1002/2016JD026315, 2017.

576   Majdi, M., Sartelet, K., Maria Lanzafame, G., Couvidat, F., Kim, Y., Chrit, M., and Turquety, S.: Precursors and

577   formation of secondary organic aerosols from wildfires in the Euro-Mediterranean region, Atmos. Chem. Phys.,

578   19(8), 5543–5569, doi:10.5194/acp-19-5543-2019, 2019.

579   Marais, E. A., Jacob, D. J., Guenther, A., Chance, K., Kurosu, T. P., Murphy, J. G., Reeves, C. E., and Pye, H. O. T.:

580   Improved model of isoprene emissions in Africa using Ozone Monitoring Instrument (OMI) satellite observations of

581   formaldehyde: Implications for oxidants and particulate matter, Atmos. Chem. Phys., 14(15), 7693–7703,

582   doi:10.5194/acp-14-7693-2014, 2014.

583   Mauzerall, D. L., Logan, J. A., Jacob, D. J., Anderson, B. E., Blake, D. R., Bradshaw, J. D., Heikes, B., Sachse, G.

584   W., Singh, H., and Talbot, B.: Photochemistry in biomass burning plumes and implications for tropospheric ozone

585   over the tropical South Atlantic, J. Geophys. Res. Atmos., 103(D7), 8401–8423, doi:10.1029/97JD02612, 1998.

586   Meller, R. and Moortgat, G. K.: Temperature dependence of the absorption cross sections of formaldehyde between

587   223 and 323 K in the wavelength range 225-375 nm, J. Geophys. Res. Atmos., 105(D6), 7089–7101,

588   doi:10.1029/1999JD901074, 2000.

589   Millet, D. B., Jacob, D. J., Boersma, K. F., Fu, T. M., Kurosu, T. P., Chance, K., Heald, C. L., and Guenther, A.:

590   Spatial distribution of isoprene emissions from North America derived from formaldehyde column measurements by

591   the OMI satellite sensor, J. Geophys. Res. Atmos., 113(2), 1–18, doi:10.1029/2007JD008950, 2008.

592   Min, K. E., Washenfelder, R. A., Dubé, W. P., Langford, A. O., Edwards, P. M., Zarzana, K. J., Stutz, J., Lu, K.,

593   Rohrer, F., Zhang, Y., and Brown, S. S.: A broadband cavity enhanced absorption spectrometer for aircraft

measurements of glyoxal, methylglyoxal, nitrous acid, nitrogen dioxide, and water vapor, Atmos. Meas. Tech., 9(2), 423–440, doi:10.5194/amt-9-423-2016, 2016.

Müller, M., Anderson, B. E., Beyersdorf, A. J., Crawford, J. H., Diskin, G. S., Eichler, P., Fried, A., Keutsch, F. N., Mikoviny, T., Thornhill, K. L., Walega, J. G., Weinheimer, A. J., Yang, M., Yokelson, R. J., and Wisthaler, A.: In situ measurements and modeling of reactive trace gases in a small biomass burning plume, Atmos. Chem. Phys., 16(6), 3813–3824, doi:10.5194/acp-16-3813-2016, 2016.

Palm, B. B., Peng, Q., Fredrickson, C. D., Lee, B. H., Garofalo, L. A., Pothier, M. A, Kreidenweis, S. M., Farmer, D. K., Pokhrel, R. P., Shen, Y., Murphy, S. M., Permar, W. Hu, L., Campos, T. L., Hall, S. R., Ullmann, K. Zhang, X., Flocke, F., Fischer, E. V., and Thornton, J. A.: Quantification of organic aerosol and brown carbon evolution in fresh wildfire plumes, P. Natl. Acad. Sci. USA, 117 (47) 29469–29477, doi:10.1073/pnas.2012218117, 2020.

Yokelson, R. J., Goode, J. G., Ward, D. E., Susott, R. A., Babbitt, R. E., Wade, D. D., Bertschi, I., Griffith, D. W. T., and Hao, W. M: Emissions of formaldehyde, acetic acid, methanol, and other trace gases from biomass fires in North Carolina measured by airborne Fourier transform infrared spectroscopy, J. Geophys. Res. Atmos., 104(D23), 30109–30125, doi:10.1029/1999JD900817, 1999.

Richter, D., Weibring, P., Walega, J. G., Fried, A., Spuler, S. M., and Taubman, M. S.: CAMS - Compact atmospheric multi-species spectrometer, Conf. Lasers Electro-Optics Eur. - Tech. Dig., 2015-Augus, 5–6, doi:10.1364/CLEO_AT.2015.ATu4J.5, 2015.

Sachse, G. W., Collins, Jr., J. E., Hill, G. F., Wade, L. O., Burney, L. G., and Ritter, J. A.: Airborne tunable diode laser sensor for high-precision concentration and flux measurements of carbon monoxide and methane, Meas. Atmos. Gases, 1433(May 1991), 157, doi:10.1117/12.46162, 1991.

Sander, S. P., Abbatt, J., Barker, J. R., Burkholder, J. B., Friedl, R. R., Golden, D. M., Huie, R. E., Kolb, C. E., Kurylo, M. J., Moortgat, G. K., Orkin, V. L., and Wine, P. H.: Chemical Kinetics and Photochemical Data for Use in Atmospheric Studies Evaluation Number 17, JPL Publ. 10-6, Jet Propul [online] Available from: http://jpldataeval.jpl.nasa.gov/, 2011.

Selimovic, V., Yokelson, R. J., McMeeking, G. R., and Coefield, S.: In-situ measurements of trace gases, PM, and aerosol optical properties during the 2017 NW US wildfire smoke event, Atmos. Chem. Phys., 19, 3905-3926, doi:10.5194/acp-19-3905-2019, 2019, 2019.

Simpson, I. J., Akagi, S. K., Barletta, B., Blake, N. J., Choi, Y., Diskin, G. S., Fried, A., Fuelberg, H. E., Meinardi, S., Rowland, F. S., Vay, S. A., Weinheimer, A. J., Wennberg, P. O., Wiebring, P., Wisthaler, A., Yang, M., Yokelson, R. J., and Blake, D. R.: Boreal forest fire emissions in fresh Canadian smoke plumes: C1-C10 volatile organic compounds (VOCs), CO2, CO, NO2, NO, HCN and CH3CN, Atmos. Chem. Phys., 11(13), 6445–6463, doi:10.5194/acp-11-6445-2011, 2011.

De Smedt, I., Theys, N., Yu, H., Danckaert, T., Lerot, C., Compernolle, S., Van Roozendael, M., Richter, A., Hilboll, A., Peters, E., Pedergnana, M., Loyola, D., Beirle, S., Wagner, T., Eskes, H., Van Geffen, J., Folkert Boersma, K., and Veefkind, P.: Algorithm theoretical baseline for formaldehyde retrievals from S5P TROPOMI and from the QA4ECV project, Atmos. Meas. Tech., 11(4), 2395–2426, doi:10.5194/amt-11-2395-2018, 2018.

Stavrakou, T., Müller, J. F., De Smedt, I., Van Roozendael, M., Van Der Werf, G. R., Giglio, L., and Guenther, A.:

631   Global emissions of non-methane hydrocarbons deduced from SCIAMACHY formaldehyde columns through 2003-

632   2006, Atmos. Chem. Phys., 9(11), 3663–3679, doi:10.5194/acp-9-3663-2009, 2009.

633   Trentmann, J., Yokelson, R. J., Hobbs, P. V., Winterrath, T., Christian, T. J., Andreae, M. O., and Mason, S. A.: An

634   analysis of the chemical processes in the smoke plume from a savanna fire, J. Geophys. Res. D Atmos., 110(12), 1–

635   20, doi:10.1029/2004JD005628, 2005.

636   Valin, L. C., Fiore, A. M., Chance, K., and Abad, G. G.: The role of OH production in interpreting the variability of

637   CH_2O columns in the southeast U.S.,, J. Geophys. Res. Atmos., 121, 478– 493, doi:10.1038/175238c0, 2016.

638   Veres, P. R., Andrew Neuman, J., Bertram, T. H., Assaf, E., Wolfe, G. M., Williamson, C. J., Weinzierl, B., Tilmes,

639   S., Thompson, C. R., Thames, A. B., Schroder, J. C., Saiz-Lopez, A., Rollins, A. W., Roberts, J. M., Price, D.,

640   Peischl, J., Nault, B. A., Møller, K. H., Miller, D. O., Meinardi, S., Li, Q., Lamarque, J. F., Kupc, A., Kjaergaard, H.

641   G., Kinnison, D., Jimenez, J. L., Jernigan, C. M., Hornbrook, R. S., Hills, A., Dollner, M., Day, D. A., Cuevas, C.

642   A., Campuzano-Jost, P., Burkholder, J., Paul Bui, T., Brune, W. H., Brown, S. S., Brock, C. A., Bourgeois, I., Blake,

643   D. R., Apel, E. C., and Ryerson, T. B.: Global airborne sampling reveals a previously unobserved dimethyl sulfide

644   oxidation mechanism in the marine atmosphere, Proc. Natl. Acad. Sci. U. S. A., 117(9), 4505–4510,

645   doi:10.1073/pnas.1919344117, 2020.

646   Warneke, C., McKeen, S. A., de Gouw, J. A., Goldan, P. D., Kuster, W. C., Holloway, J. S., Williams, E. J., Lerner,

647   B. M., Parrish, D. D., Trainer, M., Fehsenfeld, F. C., Kato, S., Atlas, E. L., Baker, A., and Blake, D. R.:

648   Determination of urban volatile organic compound emission ratios and comparison with an emissions database, J.

649   Geophys. Res. Atmos., 112(10), doi:10.1029/2006JD007930, 2007.

650   Westerling, A. L., Hidalgo, H. G., Cayan, D. R., and Swetnam, T. W.: Warming and earlier spring increase Western

651   U.S. forest wildfire activity, Science (80-.)., 313(5789), 940–943, doi:10.1126/science.1128834, 2006.

652   Wiggins, E. B., Soja, A. J., Gargulinski, E., Halliday, H. S., Pierce, R. B., Schmidt, C. C., Nowak, J. B., DiGangi, J.

653   P., Diskin, G. S., Katich, J. M., Perring, A. E., Schwarz, J. P., Anderson, B. E., Chen, G., Crosbie, E. C., Jordan, C.,

654   Robinson, C. E., Sanchez, K. J., Shingler, T. J., Shook, M., Thornhill, K. L., Winstead, E. L., Ziemba, L. D., and

655   Moore, R. H.: High Temporal Resolution Satellite Observations of Fire Radiative Power Reveal Link Between Fire

656   Behavior and Aerosol and Gas Emissions, Geophys. Res. Lett., 47(23), doi:10.1029/2020GL090707, 2020.

657   Wolfe, G. M., Marvin, M. R., Roberts, S. J., Travis, K. R., and Liao, J.: The framework for 0-D atmospheric

658   modeling (F0AM) v3.1, Geosci. Model Dev., 9(9), 3309–3319, doi:10.5194/gmd-9-3309-2016, 2016.

659   Wolfe, G. M., Nicely, J. M., Clair, J. M. S., Hanisco, T. F., Liao, J., Oman, L. D., Brune, W. B., Miller, D., Thames,

660   A., Abad, G. G., Ryerson, T. B., Thompson, C. R., Peischl, J., McKain, K., Sweeney, C., Wennberg, P. O., Kim, M.,

661   Crounse, J. D., Hall, S. R., Ullmann, K., Diskin, G., Bui, P., Chang, C., and Dean-Day, J.: Mapping hydroxyl

662   variability throughout the global remote troposphere via synthesis of airborne and satellite formaldehyde

663   observations, Proc. Natl. Acad. Sci. USA., 116(23), 11171-11180, doi:10.1073/pnas.1908931116, 2019.

664   Wotawa, G. and Trainer, M.: The influence of Canadian forest fires on pollutant concentrations in the United States,

665   Science (80-.)., 288(5464), 324–328, doi:10.1126/science.288.5464.324, 2000.

666   Yuan, B., Koss, A., Warneke, C., Gilman, J. B., Lerner, B. M., Stark, H., and de Gouw, J. A.: A high-resolution

667   time-of-flight chemical ionization mass spectrometer utilizing hydronium ions (H3O+ ToF-CIMS) for

668   measurements of volatile organic compounds in the atmosphere, Atmos. Meas. Tech., 9(6), 2735–2752,

669   doi:10.5194/amt-9-2735-2016, 2016.

670

671

672   **Figures:**
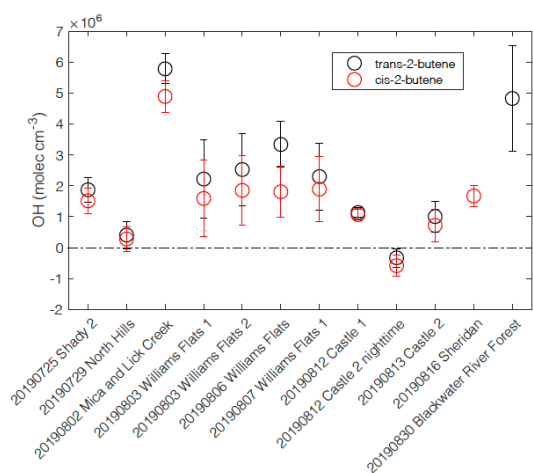
673

674   Figure 1. Estimated average OH concentrations for the plumes analyzed from the decay of trans-2-butene – propene
675   (black) and the decay of cis-2-butene – propene (red). The error bars represent the propagated uncertainties from the
676   slopes of butenes – propene decay and ozone variability within the plume.

677
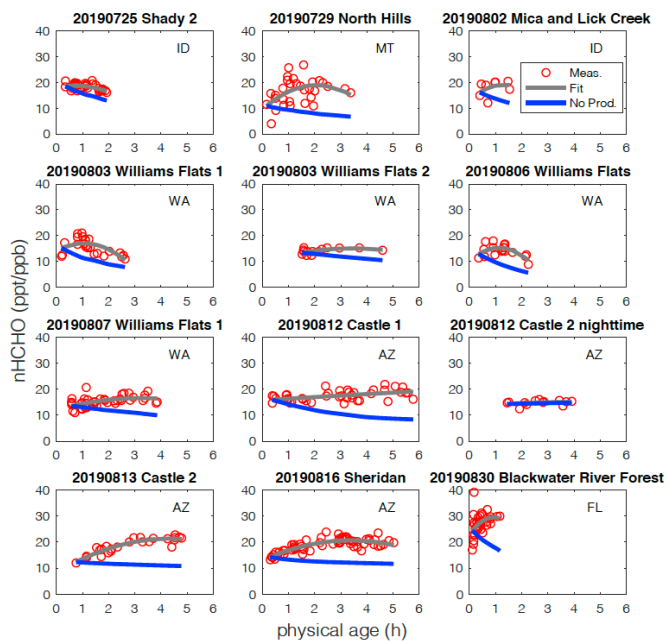
678 Figure 2. Observed nHCHO (HCHO to CO NEMR) trends (red circle), quadratic polynomial fit (pink curve), and
679 calculated decay of nHCHO trend without secondary production (blue curve) using measured photolysis rates along
680 plume physical age for the 12 wildfire plumes. The state of fire location for each fire plume is listed.

681

682
683
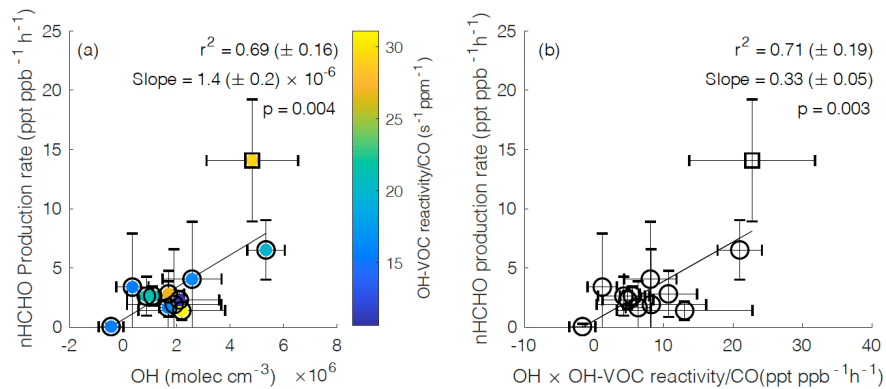
684   Figure 3. (a) Average secondary nHCHO production rate vs. average OH concentration, color-coded by normalized
685   OH-VOC reactivity, for the 12 plumes including 11 western US wildfire plumes (circles) and 1 eastern US wildfire
686   plume (square). An uncertainty weighted linear York regression (Derek, 1968) yields a slope = 1.4 ($\pm$0.2)$\times 10^{-6}$ and
687   r^2 = 0.69 ($\pm$0.16) for the 12 wildfire plumes. (b) Average secondary nHCHO production rate vs. the average product
688   of OH and OH-VOC reactivity normalized to CO (OH$\times$ OH-VOC reactivity/CO) for each plume. An uncertainty
689   weighted linear York regression yields a slope = 0.33 ($\pm$ 0.05) and r^2 = 0.71 ($\pm$0.19). The slope represents the
690   estimated effective yield α_{eff} of HCHO per VOC molecule oxidized by OH for the US wildfires. The uncertainties in
691   r^2 are from bootstrap analysis. The p-value in each panel is to evaluate if linear correlation is statistically significant
692   ($p < 0.05$).